







Spatiotemporal Variability of Rainfall and Surface Salinity in the Eastern Pacific Fresh Pool: A Joint In Situ and Satellite Analysis During the SPURS-2 Field Campaign

Nan-Hsun Chi^{1,2} , Elizabeth J. Thompson³ , Haonan Chen^{3,4} , Andrey Shcherbina¹ , Frederick Bingham⁵ , and Luc Rainville¹ 

¹Applied Physics Laboratory, University of Washington, Seattle, WA, USA, ²NOAA Pacific Marine Environmental Laboratory, Seattle, WA, USA, ³NOAA Physical Sciences Laboratory, Boulder, CO, USA, ⁴Colorado State University, Fort Collins, CO, USA, ⁵University of North Carolina at Wilmington, Wilmington, NC, USA

Key Points:

- In the eastern tropical Pacific, the integral time scale of rain is overestimated by Integrated Multi-satellite Retrievals for GPM by about a factor of two to ten all year round
- During the rainy season, sea surface salinity (SSS) integral time and length scales are shorter, approaching that of rain, and are overestimated by Soil Moisture Active Passive (SMAP)
- In the dry season, SSS integral time and length scales increase to ocean mesoscale and are captured well by SMAP

Supporting Information:

Supporting Information may be found in the online version of this article.

Correspondence to:

N.-H. Chi,
nan-hsun.chi@noaa.gov

Citation:

Chi, N.-H., Thompson, E. J., Chen, H., Shcherbina, A., Bingham, F., & Rainville, L. (2023). Spatiotemporal variability of rainfall and surface salinity in the Eastern Pacific Fresh Pool: A joint in situ and Satellite analysis during the SPURS-2 field campaign. *Journal of Geophysical Research: Oceans*, 128, e2022JC019599. <https://doi.org/10.1029/2022JC019599>

Received 23 DEC 2022

Accepted 11 OCT 2023

Author Contributions:

Data curation: Nan-Hsun Chi, Haonan Chen

Formal analysis: Nan-Hsun Chi, Haonan Chen

Funding acquisition: Elizabeth J. Thompson, Andrey Shcherbina

Investigation: Nan-Hsun Chi

© 2023. The Authors.

This is an open access article under the terms of the [Creative Commons Attribution-NonCommercial-NoDerivs License](https://creativecommons.org/licenses/by/4.0/), which permits use and distribution in any medium, provided the original work is properly cited, the use is non-commercial and no modifications or adaptations are made.

Abstract We perform a statistical characterization of the 2016–2017 SPURS-2 field campaign in situ data and coincident satellite data spanning 8°–12°N, 120°–130°W to quantify the spatial and temporal scales of variability of rain and near-surface salinity in the Eastern Pacific Fresh Pool. Observations of rain rate and near-surface to surface salinity are obtained from ships, moorings, autonomous platforms, and satellite remote sensing: Integrated Multi-satellite Retrievals for GPM (IMERG); and Soil Moisture Active Passive (NASA SMAP L3 V5). The integral length and time scales of rain and near-surface salinity vary seasonally. In the rainy season (August–October) when the Intertropical Convergence Zone (ITCZ) migrates over the SPURS-2 study site, the integral time scales of rain were about 30–60 min and those of near-surface salinity were closer to that of the rain, 1–2 days, indicating forcing by rain. Meanwhile, the zonal integral length scale of in situ near-surface salinity was twice as large as the meridional scale (50 vs. 20 km), consistent with the ITCZ's zonally-propagating and -organized rain features. The magnitude and seasonal variation of the sea surface salinity integral time scale were not captured by SMAP since the rainy ITCZ-period scales were smaller than SMAP resolution (70 km, 8-day running mean). In the dry season (February–May), the in situ rain integral time scale reduced to less than 30 min while that of the near-surface salinity increased to 1–5 days, the ocean mesoscale. IMERG overestimated the rain integral time scale by a factor of two to ten in both seasons.

Plain Language Summary Sea surface salinity (SSS) is strongly affected by local rainfall.

The Eastern Pacific Fresh Pool (EPFP) is one of the lowest salinity regions of the ocean, created by heavy precipitation under the Intertropical Convergence Zone (ITCZ) of the atmosphere. 2016–2017 SPURS-2 field observations and coincident satellite observations were used to describe how EPFP rainfall and SSS vary in time and space. Observations are obtained from ships, moorings, autonomous platforms, and satellites. The time and length scales of rain and SSS vary by season. In the rainy season the time scales of rain and near-surface salinity are similar, indicating stronger ties between the rain forcing and the salinity responses. In the rainy season the salinity spatial extent is wider in the east-west direction than the north-south direction. This is consistent with the east-west oriented pattern of rain at that time associated with the convergence of trade winds. In the dry season, observations suggest stronger influence of oceanic processes in restructuring near-surface salinity fields. The study also quantifies the differences between satellite and in-situ observations in this region. The satellite rainfall and SSS products do not resolve the details of the time and length scale variability.

1. Introduction

Quantifying and understanding the spatiotemporal variability of rain over the ocean and sea surface salinity (SSS) is critical to understanding and predicting the global hydrologic cycle. Since SSS is influenced by many multiscale atmospheric, air-sea, and oceanic processes, agreement between modeled and observed SSS is one of the key benchmarks for coupled model validation (Vinogradova & Ponte, 2017; Vinogradova et al., 2019). Though satellite-derived products describing patterns of rain and SSS variability have demonstrated absolute accuracy when compared to in situ data (Bao et al., 2019; Kao et al., 2018; Olmedo et al., 2021; Qin et al., 2020; Skofronick-Jackson et al., 2017; Tang et al., 2017) and addressed the apparent correlation between heavy rain and SSS variability (Supply et al., 2017, 2020), the resolution of globally continuous satellite products is coarse

Methodology: Nan-Hsun Chi, Andrey Shcherbina, Frederick Bingham, Luc Rainville
Resources: Elizabeth J. Thompson, Andrey Shcherbina
Software: Nan-Hsun Chi
Supervision: Andrey Shcherbina
Validation: Nan-Hsun Chi, Haonan Chen
Visualization: Nan-Hsun Chi, Haonan Chen
Writing – original draft: Nan-Hsun Chi, Elizabeth J. Thompson
Writing – review & editing: Nan-Hsun Chi, Elizabeth J. Thompson, Haonan Chen, Andrey Shcherbina, Frederick Bingham, Luc Rainville

compared to small-scale salinity structures in the ocean and even smaller time and spatial scales of individual rain freshening events. It is critical to evaluate how satellite estimates of rain rate and SSS capture spatial and temporal patterns of these variables in strongly forced or highly varying areas (e.g., Yu, 2015). In that context, this study uses recently collected data from the Salinity Processes in the Upper Ocean Regional Study-2 (SPURS-2, Lindstrom et al., 2019; Figure 1) field campaign. SPURS-2 was carried out to study rainfall-dominated surface ocean dynamics at the western edge and latitudinal center of the Eastern Pacific Fresh Pool (EPFP) to better understand the variability in the hydrologic cycle.

The EPFP and other rainfall-dominated tropical regions that span the near-equatorial belt account for a majority of earth's precipitation (Baumgartner & Reichel, 1975; Schanze et al., 2010; Trenberth et al., 2007). The EPFP's multi-scale atmospheric, air-sea, and oceanic processes lead to specific SSS annual cycles and spatial patterns that are difficult to simulate in models (A. E. A. Hasson et al., 2013; Vinogradova et al., 2019). The anomalous freshness of the tropical EPFP is created in part by excess precipitation over evaporation beneath the Intertropical Convergence Zone (ITCZ), and in part by ocean dynamics and turbulence (Alory et al., 2012; Guimbard et al., 2017; A. Hasson et al., 2019; Melnichenko et al., 2019). The ITCZ introduces persistently strong but episodic freshwater input into the upper ocean on atmospheric meso- to synoptic scales, which correspond to ocean submeso- to mesoscales (Amador et al., 2006; Fiedler & Talley, 2006). It is still not fully understood how the spatial and temporal scales of rainfall impact or contribute to the spatial and temporal scales of SSS in the EPFP, nor whether satellite products can fully capture these processes.

To quantify, understand, and validate satellite metrics of variability in the EPFP, we calculate and compare the integral length and time scales of SSS and surface rain rate from SPURS-2 field observations, and determine how well these metrics can be resolved by Soil Moisture Active Passive (SMAP) and Integrated Multi-satellitE Retrievals for GPM (IMERG) satellite products. The integral length and time scales quantify the autocorrelation of successive data points in space or time (Bingham & Lee, 2017; Tzortzi et al., 2016). Widespread and long-term in situ data are needed to calculate the in situ integral length and time scales, and to validate satellite estimates thereof.

The integral length and time scales of SSS and rain in the EPFP are expected to vary seasonally due to seasonal variations in large scale atmospheric general circulation, surface wind forcing, and ocean response (e.g., Farrar & Pludemann, 2019; Farrar & Weller, 2006; A. Hasson et al., 2019). From August to October when the ITCZ is overhead, the EPFP is under high rain and relatively low mean wind speed conditions, though gustiness does occur. During this rainy season, positive wind stress curl generates Ekman upwelling, and enhanced near-surface salinity stratification due to the input of fresh rain water is also common (Drushka et al., 2019; Iyer & Drushka, 2021a). When the ITCZ migrates to the south of the EPFP, beginning in February, the area is under conditions of low rain and moderate north-easterly trade winds. During this dry season from about February to May, both evaporation and northward Ekman transport of upper ocean water are increased in the EPFP. The prevailing surface currents migrate north and south in lock-step with the Hadley Cell (trade winds and ITCZ), and also vary in intensity with season (Guimbard et al., 2017). The eastward flowing North Equatorial Countercurrent (NECC) usually runs south of the EPFP (5°–8°N) and is more present at the SPURS-2 site during the rainy boreal summer and fall seasons when the ITCZ is farthest north. The westward flowing North Equatorial Current (NEC) typically exists north of EPFP (10°–15°N) and is present at the SPURS-2 site in the dry boreal winter and spring seasons when trade winds are overhead.

If the integral length or time scales indicated by observations are smaller than the minimum resolution of a satellite product, then this suggests that the satellite product cannot discern some of the variability in the underlying field. The EPFP features ocean submesoscale to mesoscale activity (with the time scales of hours—months, and spatial scales of several km—of 100s of km) and atmospheric mesoscale to synoptic scale forcing (temporal scales of minutes to several days, and spatial scales of several km to 100s of km). A typical operational product for SSS is the Level 3 gridded, interpolated NASA SMAP satellite product provided as an 8-day running mean centered on each day at 40 or 70 km resolution (Meissner et al., 2018). Satellite-based rain rate is offered at nominal 30-min/10 km resolution by the NASA IMERG (Skofronick-Jackson et al., 2017), though it has been found to be more representative of the 30–90 min average rate experienced over the larger area (~30 km) of the passive microwave (PMW) radiometer data sets input to the IMERG algorithms (Chiu et al., 1993; Huffman et al., 2019, 2020; Kummerow, 1998; O et al., 2017; Villarini & Krajewski, 2007; Wilheit et al., 1991).

SPURS-2 field campaign observations are used in this study to quantify how the integral length and time scales of rain and SSS evolve relative to each other in the EPFP, and how well these metrics can be resolved by SMAP and

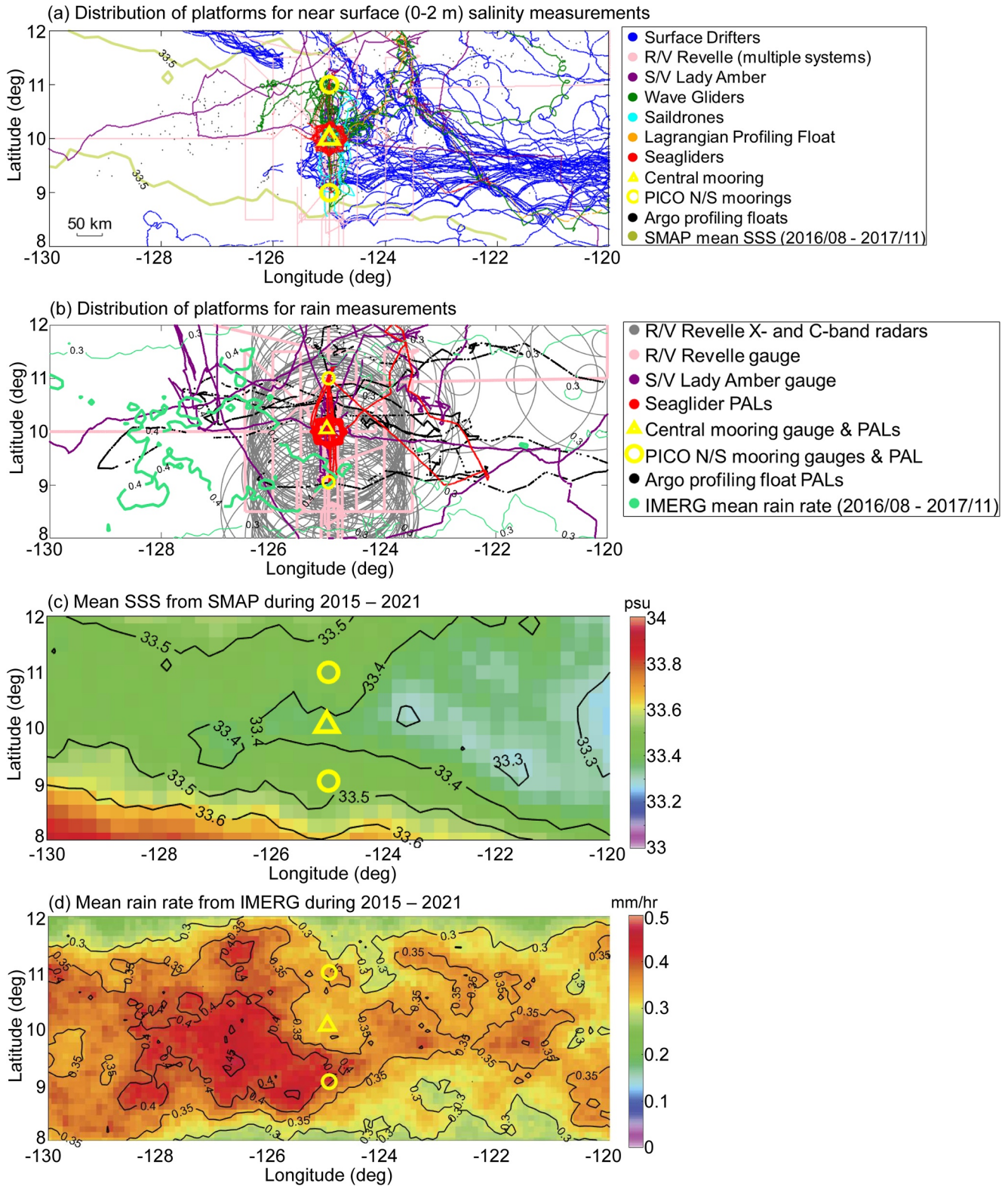


Figure 1.

IMERG satellite products. The SPURS-2 campaign collected atmospheric, oceanic, and air-sea interaction data for 15 months in an area centered at 10°N, 125°W (Bingham et al., 2019; Lindstrom et al., 2019). Satellite products and SPURS-2 in situ data are described in Section 2. Statistical methods to quantify the integral time and length scales of rainfall and SSS are described in Section 3. The integral time and space scales are computed and analyzed as a function of season in Section 4. Major findings of this study and concluding remarks are given in Section 5.

2. Data

In situ measurements from the SPURS-2 field campaign (Figure 1) and coincident satellite SSS and precipitation products are used to quantify the integral length and time scales of SSS and rain, as well as their relationship to each other. This analysis covers the 15-month period from August 2016 to November 2017 and the spatial area spanning 8°–12°N, 120°–130°W (referred to as the “SPURS-2 central area” here).

2.1. In Situ Salinity

SPURS-2 was focused around a central mooring at (10°N, 125°W) and featured nearly 200 elements of moored, piloted, and drifting uncrewed platforms deployed throughout the 15 month period, including some that were collected and redeployed near the central mooring (Bingham et al., 2019; Farrar & Plueddemann, 2019; Rainville et al., 2019; Riser et al., 2019; Shcherbina et al., 2019; Volkov et al., 2019; Zhang et al., 2019). In addition, SPURS-2 involved two separate month-long cruises by the R/V *Roger Revelle* in August–September 2016 and October–November 2017, the beginning and the end of the experiment (Bingham et al., 2019; Clayson et al., 2019; Drushka et al., 2019; Rutledge et al., 2019; Sprintall, 2019; Thompson, Asher, et al., 2019). Sampling also occurred within the SPURS-2 region during the 1-year period between *Revelle* cruises via the S/V *Lady Amber*, which visited the site and redeployed drifters, Wave Gliders, and Seagliders (Rainville et al., 2019). In total, in situ near-surface salinity data used in this study were collected from 11 different platforms (Table 1).

The salinity data cover depths between 0.1 and 2 m and span many locations over 15 months (Figure 1a). Some near-surface sensors on a few platforms that were in the field for 15 months showed salinity drifts over time related to biofouling, which have been corrected (e.g., Farrar & Plueddemann, 2019). The cross-platform salinity differences between other platforms were small and not corrected, such as those measured within an hour and within 1-km from each other between Wave Gliders and the central mooring. The Wave Gliders and the central mooring contributed the most to the spatial analysis for the 15-month period. The two platforms had an RMSD and bias 0.03 and <0.01 psu, respectively. The RMSD for the all cross-platform salinity differences is 0.16 psu. The differences stem from measurements being located in different places relative to salinity fronts and from measurements being from different depths in the presence of strong vertical salinity stratification. These salinity differences are not considered obstacles for the spatial or temporal decorrelation time scale calculations. Most of the salinity data came from a few platforms that mainly moved together or were always arranged near other platforms along a zonal or meridional axis (ex. central mooring, Wave Gliders, drifters, ship data). Most of the integral length scale calculations (Section 3.2) use data from platforms with smaller cross-platform differences (Wave Gliders, central mooring, Seagliders). The statistical methods in deriving the integral length scale (Section 3.2) were not sensitive to these small cross-platform biases.

The multi-platform SPURS-2 salinity observations were averaged and gridded into a homogenous data set with 1-km spacing and 1-hr temporal resolution. Hereafter, we refer to this gridded near-surface salinity data set as the “SPURS-2 1 km-1 hr salinity data.” Most data (shown in Figure 2) were collected at or near the central mooring, between 9° and 11°N along 125°W. The Lagrangian float and drifters drifted eastward away from the SPURS-2 central area, in the NECC along the south side of the SPURS-2 central area, or otherwise, they drifted westward in the NEC along the north side of the SPURS-2 central area. Surface currents in this region are strong (20–30 cm/s, e.g., Guimbard et al., 2017), so drifting instruments deployed here typically left the SPURS-2 central area within

Figure 1. Distribution of platforms in the SPURS-2 central area for (a) near surface salinity and (b) rain measurements during SPURS-2. The 33.5 psu contour line in panel (a) is the mean Soil Moisture Active Passive (SMAP) sea surface salinity (SSS) during August 2016–November 2017 (SPURS-2 period). The 0.3 mm/hr (thin green line) and 0.4 mm/hr (thick green line) contours in panel (b) are based on averaged 30-min Integrated Multi-satellite Retrievals for GPM (IMERG) rain rates during August 2016–November 2017 (SPURS-2 period). The climatological mean SSS (c) and rain rate (d) are computed from 2015 to 2021 using SMAP and IMERG products, respectively. The SPURS-2 central mooring (10°N, 125°W) locations and Instrumentation for Continuous Observations moorings are shown by yellow triangle and yellow circles, respectively.

Table 1

The Direct Oceanic Measuring Platforms Used in This Study, Including Numbers and Depths Used in the Analysis

#	Platforms	Number of platforms/deployments of each type (location)	Depths used in analysis
1	WHOI mooring ^a	1 (10°, 125°W)	1 m
2	PMEL PICO profiling CTD mooring ^{a,b}	2 (9°N, 125°W; 11°N 125°W)	3–5 m average ^b
3	Mixed layer Lagrangian profiling float ^c	1 (changing location)	1–2 m
4	Surface drifters ^c	6 types, >100 drifters (changing locations)	0.05–2 m depending on type
5	Seaglider ^d	5 (changing locations)	1–2 m
6	Wave gliders ^d	3 (changing locations)	0.1–0.4 m
7	Saildrone ^d	2 (changing locations)	0.6 m
8	Surface salinity snake ^c	2 R/V Roger Revelle cruises in 2016 and 2017 (changing locations)	0.1–0.2 m
9	Surface salinity profile ^c (SSP)		0.12, 0.23, 0.54, and 1.1 m
10	Underway salinity profiling system ^c (USPS)		2 m (thought to be representative of 0.5 m depth based on comparison to SSP)
11	Lady Amber profiling system ^c (LAPS)	4 R/V Lady Amber cruises in 2016 and 2017 (changing locations)	1 and 2 m

Note. The superscript numbers next to the platform names represent the type of this platform described below.

^aEulerian type platforms. ^cLagrangian type platforms. ^dUncrewed vehicles that navigate along defined routes. ^eShip-based platforms, that is, R/V *Roger Revelle* or S/V *Lady Amber*. ^bPMEL CTD mooring data were not collected above 2 m so were not used in the near-surface 1-km 1-hr gridded data set, but its average data from 3 to 5 m were used in Figure 7.

1 week. All in situ salinity data above 2 m are compared to SMAP SSS and used to compute integral length scale, while only the fixed-location salinity data are used to estimate the integral time scale.

2.2. Satellite Sea Surface Salinity

In this study, we use NASA SMAP Level 3 Version 5 SSS (Meissner et al., 2018) to compute integral length and time scales of SSS. This product is provided on a $0.25^\circ \times 0.25^\circ$ spatial grid (approx. 26 km \times 27 km at 10°N), using a 70-km spatial covariance and an 8-day sliding temporal window on each day.

In order to quantify how well SMAP can describe spatiotemporal variability of in situ salinity during SPURS-2 field campaign, the in situ measurements are first compared to the SMAP product in a validation exercise in Figure 3. The RMSD and R^2 are 0.31 and 0.75, respectively, consistent with previous comparisons from 2016 to 2017 between satellite SMAP SSS and Tropical Atmosphere Ocean/Triangle Trans Ocean Buoy Network Moored Array mooring 1-m salinity data, whose RMSD and R^2 were 0.26 and 0.70 (Bao et al., 2019). SPURS-2 salinity in situ values are often slightly higher than SMAP SSS, as the centroid of points is just below the 1:1 line. The differences could be due to sub-footprint variability sampling errors between satellite and in situ products, the differences in depths they measure, or the patchy nature of rainfall (Bingham, 2019; Drucker & Riser, 2014; Thompson, Asher, et al., 2019). The slight SMAP SSS negative bias compared to SPURS-2 in situ 0.1–2 m salinity data is consistent with the fact that SMAP senses lower SSS at the skin level following rainfall than would subsurface 0.1–2 m salinity in situ sensors. This supports findings from other studies that the near-surface haline stratification is prominent under frequent rainfall in the EPFP region (Reverdin et al., 2012, as well as Drushka et al., 2019; Iyer & Drushka, 2021b using SPURS-2 data).

2.3. In Situ Meteorology

The integral time scale of rain was only calculated from three moorings (Figure 1b). On the central mooring, three self-siphoning rain gauges sampled rain accumulation over 1-min periods, from which a 1-min time series of average rain rate was constructed (Farrar & Plueddemann, 2019). A surface self-siphoning gauge was also deployed on each of the two Pacific Marine Environmental Laboratory (PMEL) Platform Instrumentation for Continuous Observations (PICO) moorings located 1° to the south and north of the central mooring. Fourteen other platforms measured rainfall during SPURS-2 (Figure 1b) but their spatial and/or temporal extent was not

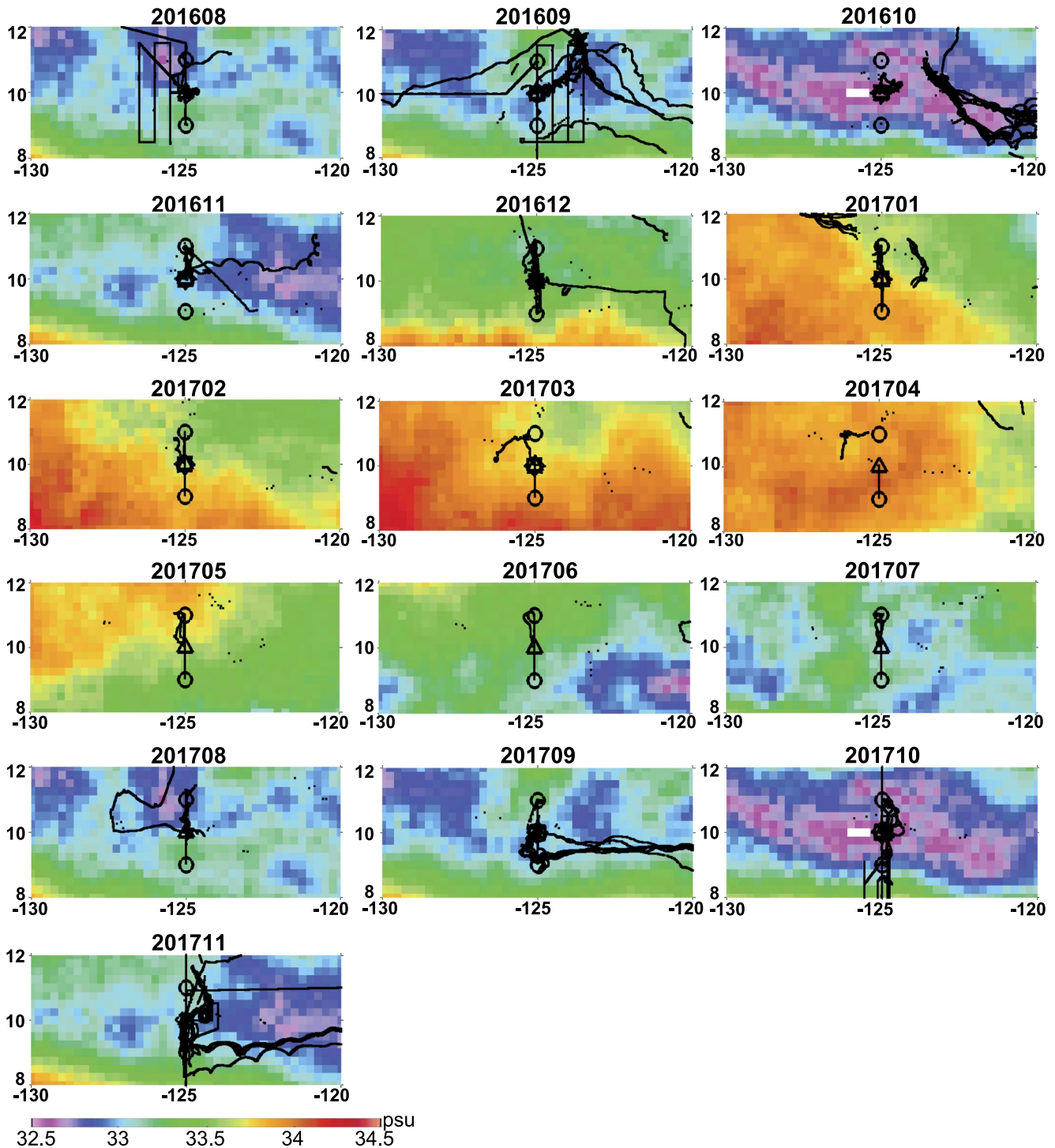


Figure 2. Soil Moisture Active Passive (SMAP) monthly averaged sea surface salinity (colors, with scale at bottom left) overlaid with SPURS-2 1 km-1 hr data (black lines and dots on top of the SMAP map) whenever available in the same month within (130°W–120°W, 8°N–12°N). The black triangle is the location of the SPURS-2 central mooring. The black circles are the locations of the PMEL PICO moorings. Different panels correspond to different months as given in the text at the top of each panel.

dense enough in each 30-day time window used for the integral length and time scale calculations in this study (see Section 3 for calculation details). We note and plot these other rain data sets here even though they do not contribute to this analysis because the null result can inform planning of future experiments. Time series of vector wind data from the central mooring anemometer were also analyzed.

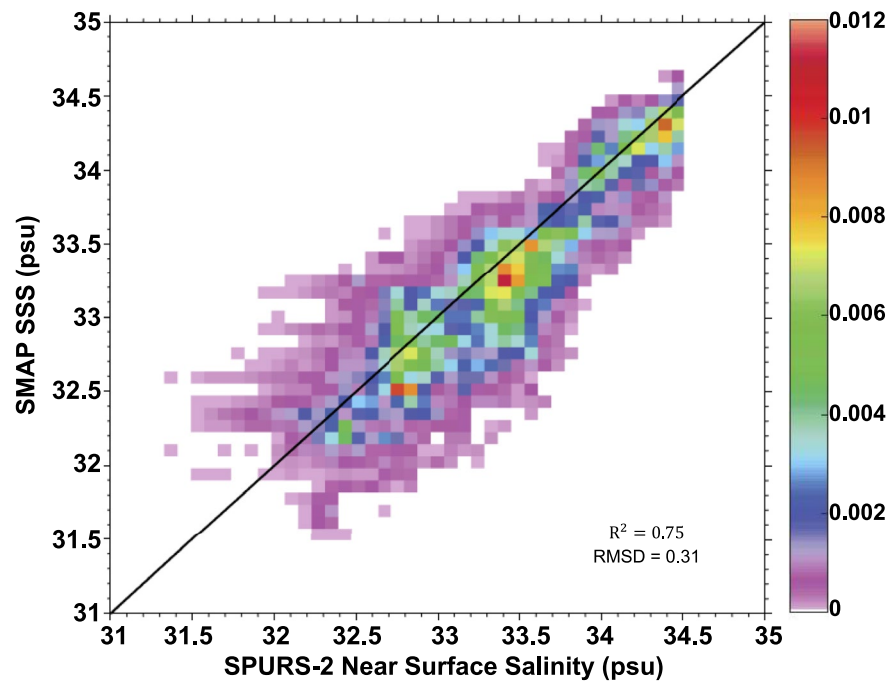


Figure 3. Two-dimensional histogram of Soil Moisture Active Passive 8-day running mean sea surface salinity (70 km resolution product, V5.0) and SPURS-2 1 km-1 hr near surface salinity data between August 2016 and November 2017. The 2-D histogram is normalized by the total number of realizations (144,219).

2.4. Satellite Precipitation

The IMERG V06 rain rate product is used to compute both the integral length and time scales of rain. IMERG is produced by NASA using a constellation of satellite-based estimates (Huffman et al., 2019, 2020). The IMERG product is created by intercalibrating, merging, and interpolating various PMW-based precipitation retrievals, together with PMW-calibrated infrared-based precipitation estimates. The “Final Run” of IMERG V06 is used here. It incorporates land-based gauge corrections over land but not oceanic, mooring- or island-based gauge corrections over the ocean. The nominal temporal resolution of IMERG is 30 min, and the spatial resolution is $0.1^\circ \times 0.1^\circ$. However, as mentioned in the introduction, prior studies suggest that IMERG values are most representative of 30–90 min average rates over larger areas, such as the area of the input PMW beamwidths, ~ 30 km (Chiu et al., 1993; Huffman et al., 2019, 2020; Kummerow, 1998; O et al., 2017; Villarini & Krajewski, 2007; Wilheit et al., 1991).

3. Methods

3.1. Temporal Scale Analysis

We use the salinity and rain time series from the three SPURS-2 moorings (Table 1, Figures 1a and 1b), the SMAP L3 V5 8-day SSS data, and IMERG V06 rain data in the SPURS-2 central area to estimate the autocorrelation ρ as a function of temporal lag τ . The integral time scale is then defined as:

$$T = \int_0^{\tau_0} \rho(\tau) d\tau \quad (1)$$

where τ_0 is the first zero crossing of the autocorrelation function $\rho(\tau)$. The autocorrelation function and therefore also the integral time scale are computed every 24 hr from a rolling 30-day window centered on the day. For this calculation, $d\tau$ in Equation 1 is 5-min for the salinity data collected at the central mooring and 10-min at the two PICO moorings. The near-surface salinity data are gridded at 1 hr-1 km for integral length scale calculation. These details for how integral time scale was computed from in situ measurements are summarized in Table 2. The autocorrelation function and integral time scales of satellite SSS (SMAP) and rainfall (IMERG) are also computed with these same time windows (30-day) at each grid point within the SPURS-2 central area. The

Table 2

Summary of the Spatial and Temporal Resolutions of Salinity and Rain Rate Data Used in This Study, As Well As the Spatial and Temporal Scales Used for Computing the Semi-Variograms and Integral Time/Length Scales

	SPURS-2 in situ 0–1 m S	SMAP SSS	IMERG rain	SPURS-2 central mooring in situ rain rate
Spatial grid used in calculations	Point measurements regridded to 1-km	70-km product, regridded to 25-km	10-km product	Point measurements
Temporal resolution used in calculations	1 s–30 min point measurements regridded to 1-hr for semi-variogram calculation; or 5-min (central mooring) and 10-min (two PMEL moorings) for integral time scale calculation	8-day running mean product centered on each day, that is, daily products	30-min product	1-min data
Semi-variogram calculation	Data set is sampled at “A” intervals. For each sample, a semi-variogram is calculated at a spatial resolution of “B” using Equation 2. The sampled results of each spatial separation bin is then averaged with a moving 30-day window centered on each day			N/A
	A/B			
	48-hr/2-km	24-hr/25-km	30-min/10-km	
Semi-variogram calculation	For each 48-hr sample, we calculated a semi-variogram result at a spatial resolution of 2-km using Equation 3. The results at each spatial separation bin were then averaged with a moving 30-day window centered on each day	For each 24-hr sample, we calculated a semi-variogram result at a spatial resolution of 25-km using Equation 3. The results at each spatial separation bin were then averaged with a moving 30-day window centered on each day	For each 30-min sample, we calculated a semi-variogram at a spatial resolution of 10-km using Equation 3. The results at each spatial separation bin were then averaged with a moving 30-day window centered on each day	N/A
Integral length scales	Calculated with 30-day averaged semi-variograms			N/A
Integral time scales	Calculated every 24 hr with a 30-day period of data			

mean, 10th, and 90th percentile values of the integral time scale are computed as a function of time across the SPURS-2 central area. It should be noted that the temporal resolution of the observations may have an impact on the computed integral time scales, especially when the two are comparable (as is the case for the rain integral time scales, see Section 4.2.1 below). Sensitivity tests are provided in Supporting Information S1.

3.2. Spatial Scale Analysis

In situ observations were sparsely and non-uniformly distributed (Figures 1a and 2 for salinity, Figures 1b and 4 for rain), so calculation of the autocorrelation function with these data in the spatial dimension is less straightforward than for point measurements in the time dimension. We therefore use semi-variogram analysis, described below, to estimate the integral length scale. Spatial scale analysis is only applied to in situ and satellite-based SSS, and satellite precipitation; the spatial range of the point and radar measurements of rain was too small to comprehensively compute the integral spatial scale in the EPFP (Figure 4).

3.2.1. Semi-Variogram Analysis

The semi-variogram of a spatially varying parameter s is defined as the mathematical expectation (or mean) of the squared difference between pairs of values $s(x)$ and $s(x + h)$ separated by a distance h (Journel & Huijbregts, 1978; Kitanidis, 1997):

$$\gamma(h) = \frac{1}{2} E\{[s(x) - s(x + h)]^2\} \quad (2)$$

The separation, h , is one-dimensional (e.g., longitude or latitude) in this study, but it can also be multidimensional vectors (e.g., latitude-longitude).

The semi-variogram is directly related to spatial autocorrelation $\rho(h)$ as $\gamma(h) = \sigma^2 (1 - \rho(h))$, where $\sigma^2 = E\{(s(x) - \mu)^2\}$ is the variance, and $\mu = E\{s(x)\}$ is the mean, both assumed to be stationary. Unlike

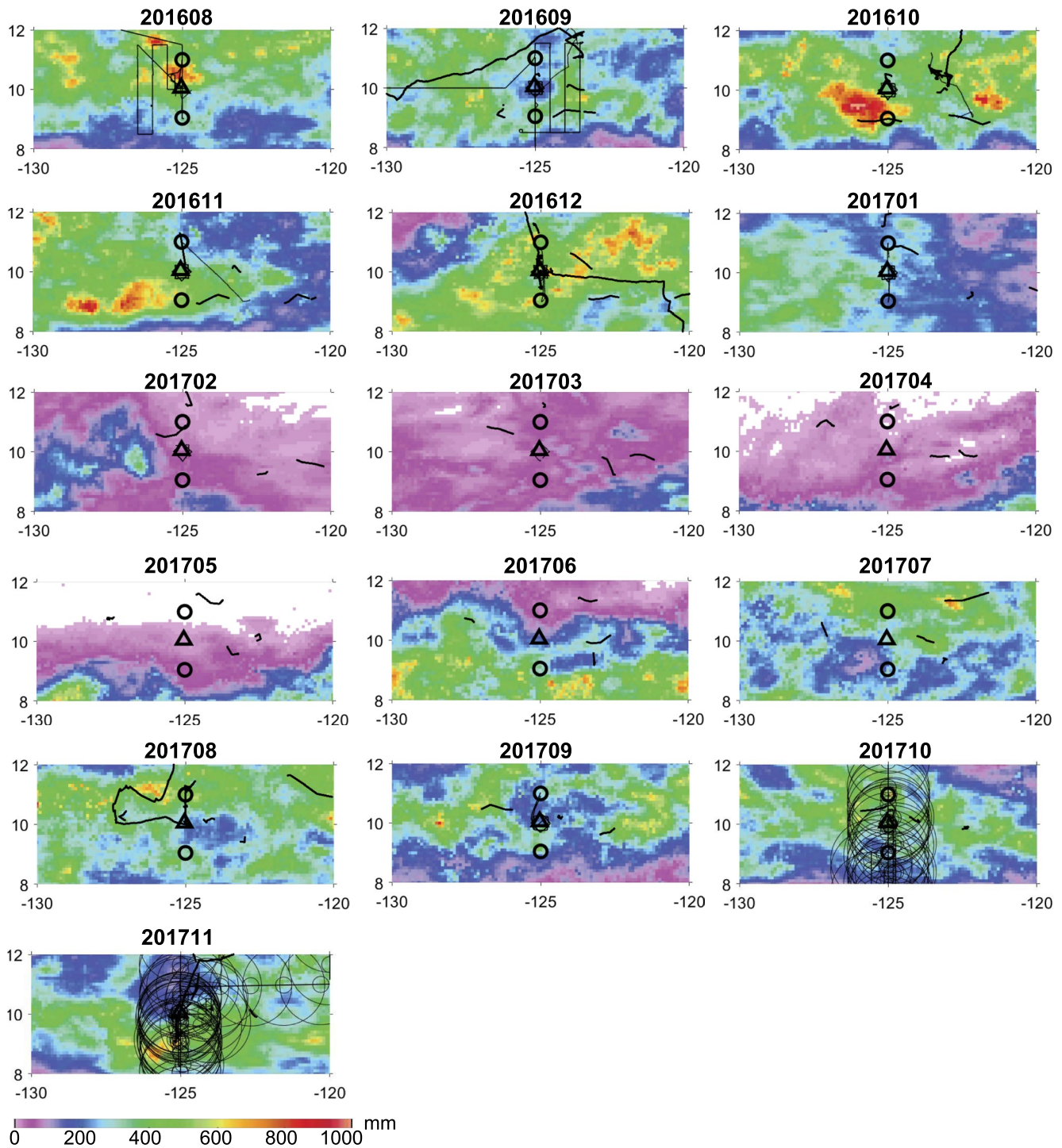


Figure 4. As in Figure 2, but for Integrated Multi-satellite Retrievals for GPM V06 monthly rainfall. The larger black circles (150-km radius) and collocated smaller circles (30-km radius) indicate the coverage ranges of SEA-POL (SEA-going POLarimetric) C-band radar and X-band marine radar deployed aboard *R/V Roger Revelle* during October and November 2017 (second cruise of SPURS-2).

autocorrelation, however, computation of the semi-variogram does not require a-priori knowledge of σ^2 or μ , and therefore is preferable for unevenly distributed observations. In practice, no two pairs of observations would be separated by the exact same distance h , so a separation window $[h - \delta h/2, h + \delta h/2]$ is used, with the window width δh selected to ensure enough observation pairs in each window for statistical stability. The semi-variogram in Equation 2 is then estimated on an equally spaced separation grid h_i , with the resolution $h_{i+1} - h_i = \delta h$.

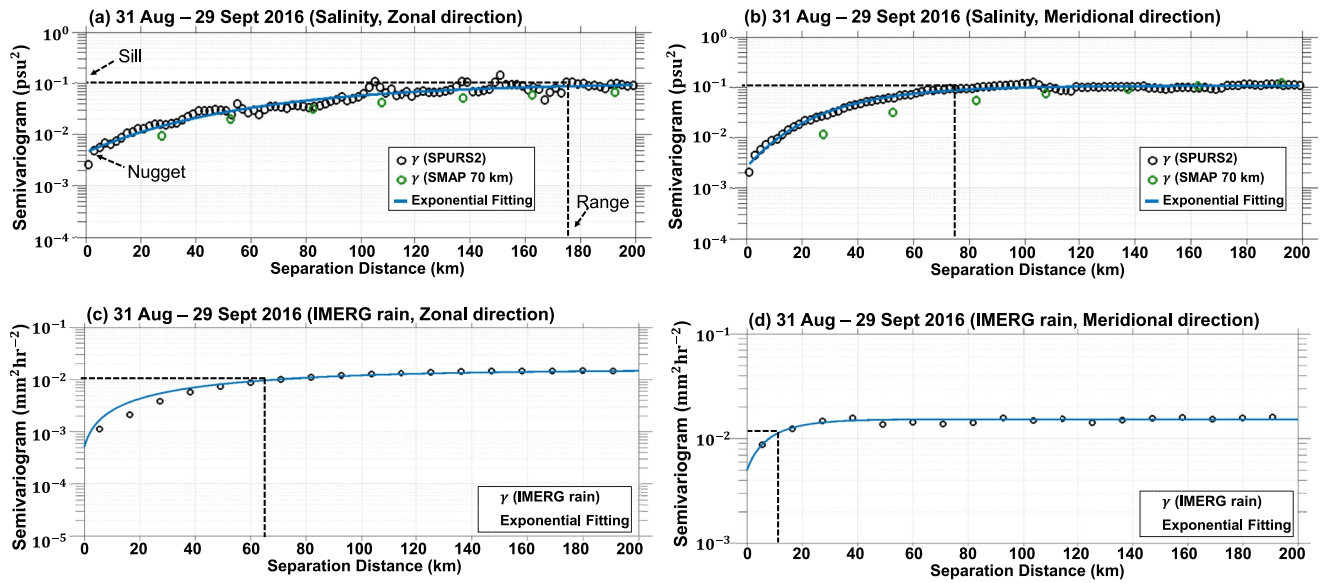


Figure 5. Examples of the estimated (circles) and modeled (lines) semi-variograms of Soil Moisture Active Passive (SMAP) sea surface salinity (SSS), SPURS-2 salinity, and Integrated Multi-satellitE Retrievals for GPM (IMERG) rain over a 30-day period between 31 August and 29 September 2016: (a) zonal and (b) meridional directions of SMAP SSS and SPURS-2 salinity; (c) zonal and (b) meridional directions of IMERG rain. The black circles are from (a, b) SPURS-2 1 km-1 hr salinity and (c, d) IMERG rain data. The green circles in panels (a, b) are for SMAP 70-km resolution SSS. The blue lines are the exponential fit curves (Equation 4) to the in situ data. The vertical and horizontal dashed black lines in each panel indicate the estimated range and sill from each exponential fit curve to the in situ data.

For a normally distributed variable, a simple ensemble average $\bar{s} = \frac{1}{N} \sum_{i=1}^N s_i$ could be used as an estimate of expectation $E\{s\}$. In practice, however, the data distribution is often not normal and can be contaminated by outliers or heavy tails. Therefore, we employ a more robust semi-variogram estimator proposed by Cressie and Hawkins (1980):

$$\gamma(h) = \frac{\frac{1}{2} \left(\frac{1}{N(h)} \sum_{N(h)} |s(x_i) - s(x_j)|^2 \right)^2}{0.457 + \frac{0.494}{N(h)} + \frac{0.045}{N(h)^2}} \quad (3)$$

where $N(h)$ is the number of available sample pairs separated by distance of h .

To facilitate interpretation of the semi-variograms in Equation 3, we approximate them with parametric model functions, such as the exponential model (Doney et al., 2003; Journel & Huijbregts, 1978):

$$\gamma_{exp}(h) = c_0 + (\sigma^2 - c_0) \left(1 - e^{-\frac{h}{r_e}} \right) \quad (4)$$

In the interpretation of the exponential semi-variogram, the “nugget” c_0 corresponds to the unresolved, subscale variance or measurement error, the “sill” σ^2 is the variance of the variable field, r_e describes the e-folding scale of the field toward decorrelation. The range, r , is the separation at which the semi-variogram reaches 95% of the sill (Figure 5a). Two additional parametric models, spherical and Gaussian, were also tested to interpret the semi-variograms. These showed similar results. The exponential model is chosen for its closest representation of the nugget and at smaller separation distances. Parameters of the exponential semi-variogram model in Equation 4 are estimated using a least square fit of semi-variograms computed from Equation 3 on a log-10 scale following the approach in Schwanghar (2020). For an exponential semi-variogram, the integral length scale can then be computed analytically as:

$$L = \int_0^{\infty} \rho(h) dh = \int_0^{\infty} (1 - \sigma^{-2} \gamma_{exp}(h)) dh = (1 - \sigma^{-2} c_0) r \quad (5)$$

3.2.2. Application of Semi-Variogram to In Situ Salinity

In order to calculate the spatial scale statistics, simultaneous measurements are needed. Few samples were taken simultaneously and therefore a “simultaneity window” was needed, within which we call the measurements “simultaneous” for the purposes of Equation 3. This improves statistics, but aliases spatial and temporal statistics to some extent. As a compromise, we chose 48 hr as a “simultaneous window.” Every 48 hr, we apply Equation 3 to the available near-surface in situ salinity data pairs and accumulate them for each separation bin, δh , in zonal and meridional directions using the SPURS-2 1 km-1 hr salinity data (Table 2). For each rolling 30-day window centered on the day, the accumulated pairs from each spatial separation bin are averaged to produce the mean semi-variogram using Equation 3 over 30 days. Then the exponential model is fit to the semi-variograms for the parameters in Equation 4 and the integral length scale is computed as in Equation 5. Each 30-day mean semi-variogram estimated by Equation 3 is at 2-km separation resolution (δh) centered from 1 to 199 km (Figure 5).

Statistical tests are used for quality control for integral length scales derived from semi-variograms. First, a minimum of 100 valid salinity pairs are required at each spatial separation bin—a stricter criterion than the practical rule of Journel and Huijbregts (1978) who used a minimum of 30 valid pairs. Second, more than 80% of valid gridded spatial separation bins are required to apply model fit in Equation 4. Third, the coefficient of determination, R^2 , of the model fit to the semi-variogram must exceed 0.9.

3.2.3. Application of Semi-Variogram to Satellite SSS and Rain

Similar to Section 3.2.2, we apply the same semi-variogram calculation, exponential model fit, and integral length scale calculation to SMAP L3 V5 8-day running mean daily SSS data resampled to 0.25° , and on IMERG 30-min, 0.1° resolution rain data over the same SPURS-2 central area (Table 2). The first two quality control steps in Section 3.2.2 are not required in fitting the semi-variograms since the satellite products are on regular grids without holes. The lower resolution of SMAP data reflects on the lower number of points for the exponential model to fit the semi-variograms (green vs. black circles in Figures 5a and 5b).

4. Results

4.1. Annual Cycle of Rainfall and Near-Surface Salinity: In Situ and Satellite

Consistent with the climatology, both precipitation, and winds exhibit seasonal variability in the EPFP (Figures 4 and 6, Guimbard et al., 2017; Melnichenko et al., 2019). From August to October, the “rainy season,” when the ITCZ is overhead or just north of the central mooring, the site receives a large amount of rainfall and weak (0–8 m/s) winds. Wind direction is also variable during this period. SSS in the EPFP is fresher during the rainy season (Figure 2, e.g., Melnichenko et al., 2019). The rain falls in patchy areas, even in monthly average maps (Figure 4) and a 7-year average map (Figure 1d). In an instantaneous sense, rain cells may be as small as 1–10 km when unorganized or isolated (Rutledge et al., 2019; Schumacher & Houze, 2003; Thompson, Asher, et al., 2019; Trivej & Stevens, 2010), or can exceed 150 km in width when organized in mesoscale convective systems and/or easterly waves (Cifelli et al., 2007; Houze et al., 2015; Petersen et al., 2003). SMAP SSS decreases during the rainy season in somewhat patchy areas that are similar to rainfall except the area of salinity decrease is slightly larger and less peaked (smoother spatially, Figures 2 and 4). From November to January at the central mooring site, there is a transitional period from rainy to little rainfall while light variable winds transitioned to steadily northeasterly winds at higher speeds than observed in the rainy season. When the ITCZ is well south of 10°N from February to May, the central mooring site receives little rainfall and has strong and steady northeasterly trade winds (6–9 m/s), with correspondingly saltier SSS. The salty SSS patterns in this dry trade wind period appear larger and smoother than the smaller scale fresh patches evident in the rainy season.

4.2. Time Scales of Variability

4.2.1. Rain

Figure 7 shows the integral time scales of SMAP SSS and IMERG rain rate over the SPURS-2 central area as well as in situ near-surface salinity and rain rate at the three moorings.

The mean integral time scale of the in situ rainfall at the central mooring during the rainy season and transitional period between rainy to little rain (June–January) was 39 min, with values as high as 67 min, while it was much shorter, 19 min mean, in the dry season (February–May). These time scales are within the range of the time scales

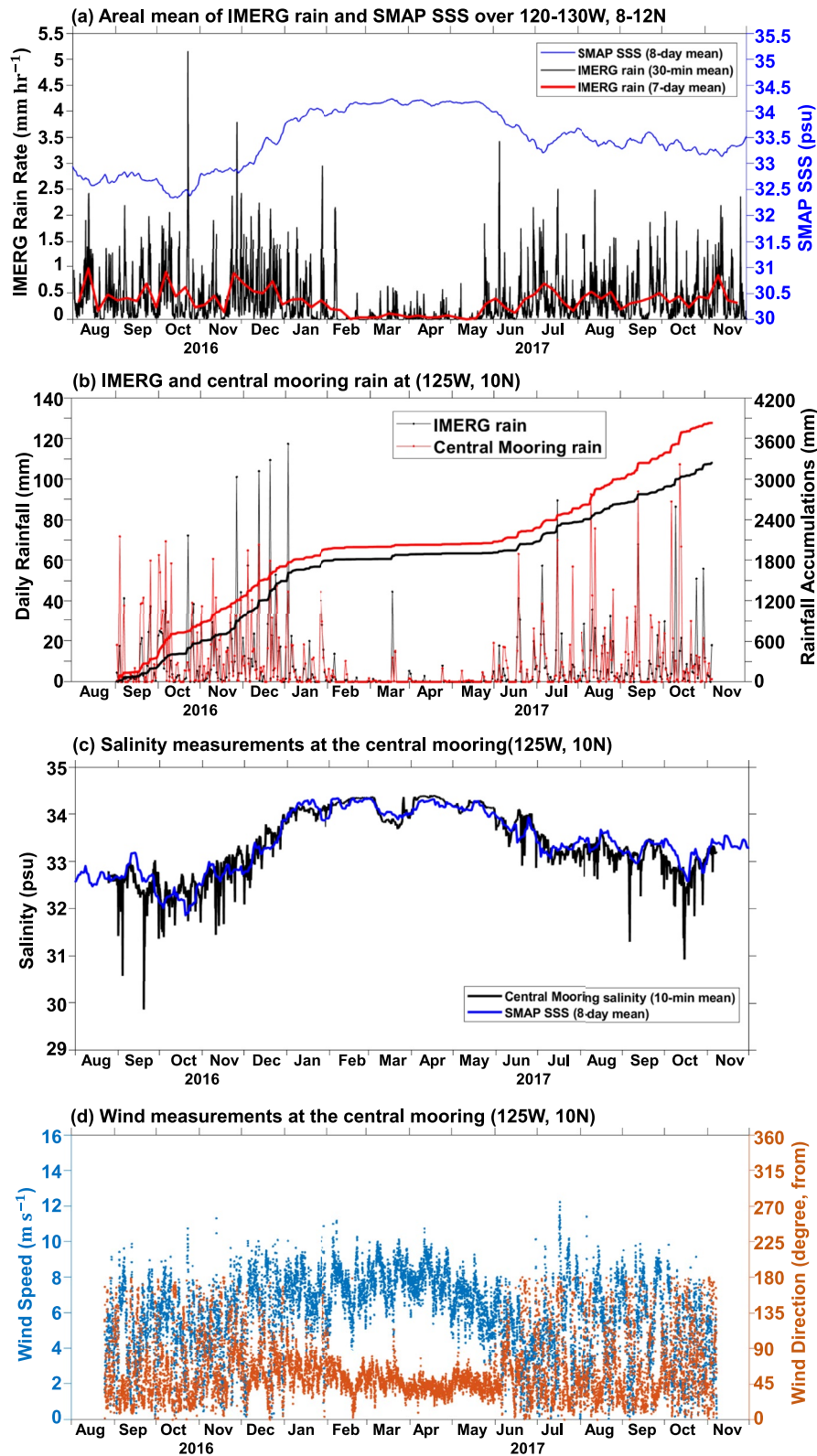


Figure 6.

of the atmospheric cloud and mesoscale processes, which have been shown to be the dominant mode of variability of EPFP rainfall (Cifelli et al., 2008; Houze et al., 2015). For all three moorings, the integral time scale of rain decreases from the boreal summer/fall rainy season to the winter/spring low-rain season, respectively (Figure 7), indicating shorter duration of rain events in the low rain season which is consistent with climatology (Cifelli et al., 2008). The time scale decreases when the ITCZ is further away from the area. This is understandable since rain cell frequency, size, and therefore lifetime will decrease when the ITCZ, the main precipitation forcing mechanism in this region, is further away (Figures 4, 6, and 7, Cifelli et al., 2007).

The integral time scale of IMERG rain is about two to ten times longer than that of in situ rain measurements, but time scales estimated from both data sources show similar seasonal trends. The seasonal variations of rain integral time scales from IMERG appear tied to the location of the ITCZ and consistent with in situ data time scales for reasons already explained. In the rainy season, the mean IMERG integral time scales over the SPURS-2 central area (Figures 7b and 7e, dark blue solid line with circles) and at the central mooring location (Figures 7b and 7f, light blue solid line with circles) are generally 2–5 hr. In the meantime, the in-situ rain integral time scales are usually 30–60 min, at or below the 10th percentile value of the IMERG integral time scale estimates. During the rain-free periods (particularly during the dry season), the in situ estimate of the integral length scale shrinks to under 30 min and is overestimated by about a factor of two to ten by IMERG. The consistent overestimation of rain integral time scale by IMERG is likely symptomatic of the relative coarseness of the 30-min, 10-km IMERG product, which misses sub-footprint and sub-time step variability in tropical rainfall. For instance, EPFP rain details are missed between infrequent PMW overpasses and due to limitations in the ability of IR data to comprehensively inform the output of IMERG and its algorithms. The impact of morphing different satellite rainfall retrievals across time steps when no satellite overpass occurs (Huffman et al., 2019) and the variability between different satellite sensors used by IMERG, is neglected in computing the integral time scales. As a result of these limitations, rain's fine scale temporal variability (<30–90 min) and the resulting integral time scale estimate is not well-quantified by IMERG compared to in situ estimates.

4.2.2. Near-Surface Salinity

The in situ near-surface salinity integral time scale as measured at the central mooring is shorter during the rainy season than the dry season, 1–2 days versus 1–5 days (Figure 7a). During the rainy season the near-surface salinity was often impacted by strong and episodic rainfall (Figure 6). In fact, the in situ integral time scales of rain and near-surface salinity converge (larger for that of rain and smaller for that of salinity) during the rainy season, suggesting stronger ties between the rain forcing and near-surface salinity response. Because of the high-rain and relatively low-wind conditions of the rainy season, near-surface salinity stratification by rain was common (Drushka et al., 2019; Iyer & Drushka, 2021a; Reverdin et al., 2020). These fresh near-surface stable layers can remain at the surface for up to about 1 day (Drushka et al., 2016, 2019; Thompson, Moum, et al., 2019), particularly if the wind speed is low enough (Thompson, Moum, et al., 2019, who called these features “rain layers”) or if preexisting stratification below the fresh layer contributes to the stability of the surface layer (Iyer & Drushka, 2021a). Thus, stratification generated by rain extends the timescale of near-surface salinity response compared to those of the rain forcing. This, in addition to other ocean dynamical processes that redistribute freshwater from rain in the ocean, could contribute to the salinity integral time scale converging toward that of rain in the rainy season, but still remaining larger than the integral timescale of rain.

During the dry season the observed integral time scales of near-surface salinity are larger and more variable (1–5 days). The integral times scales of in situ rain and near-surface salinity diverge during the dry season, suggesting the variability of near-surface salinity is dominated by ocean processes rather than the few episodic rain events occurring in the dry season. The fast (~1 month) swing toward greater near-surface salinity integral time scales during boreal spring may be associated with an increase in intraseasonal variability of westward moving mesoscale ocean eddies within the NEC near 10°N latitude (Farrar & Weller, 2006; A. Hasson et al., 2019). These results suggest that, during dry seasons, oceanic mesoscale processes dominate the temporal scale of near-surface salinity variations.

Figure 6. (a) Areal mean Integrated Multi-satellitE Retrievals for GPM (IMERG) V06 rain rates at 30-min (black) and 7-day (red) time scales and 8-day running mean (blue) Soil Moisture Active Passive (SMAP) L3 V5.0 sea surface salinity (SSS) over the SPURS-2 time period and domain (130°–120°W, 8°–12°N). The 7-day mean of IMERG rain is computed by averaging all the 30-min IMERG rain rates during each 7-day window. (b) Central mooring (125°W 10°N) daily rainfall (thin) and total (thick) rain accumulation from gauge and collocated IMERG grid data. Mooring data are in red and IMERG are in black. (c) Central mooring (125°W 10°N) salinity from 10-min 1-m depth in situ data and collocated 8-day running mean daily 70-km SSS SMAP grid data. (d) Central mooring (125°W 10°N) hourly mean wind speed and direction (from, with 0° meaning from the north).

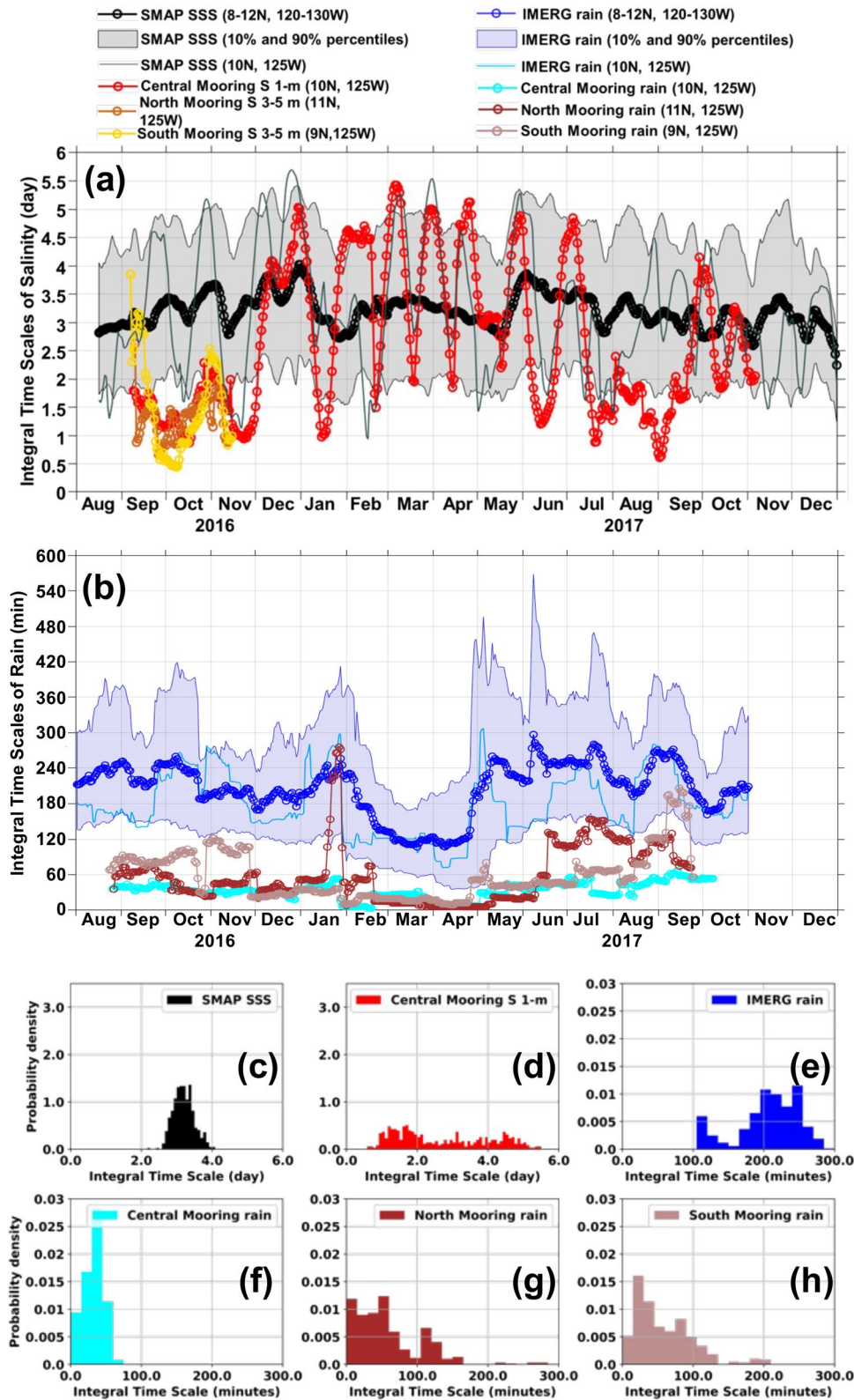


Figure 7.

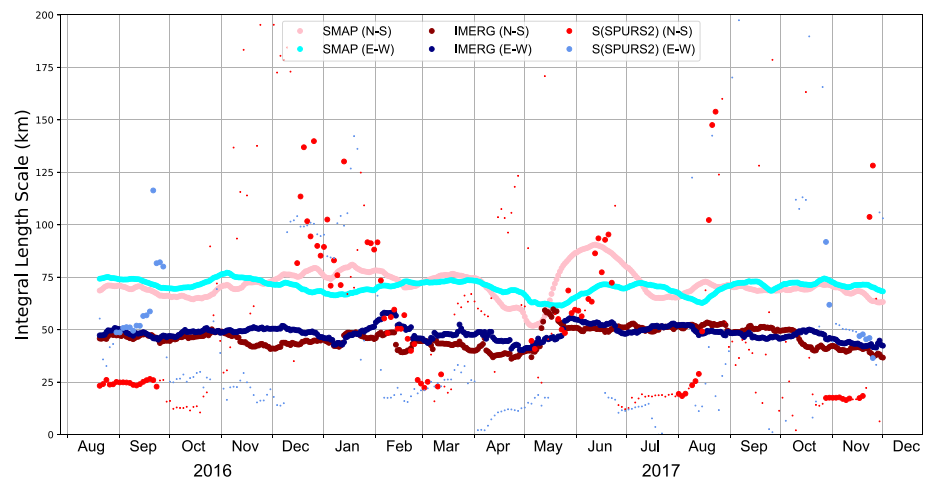


Figure 8. Integral length scales of SPURS-2 unified data set in the zonal (big cornflower blue circles) and meridional (big red circles) directions from a rolling 30-day window centered on the day. The small blue and red dots are the integral length scale estimates which did not pass the statistical tests described in Section 3.2.2 because they either had insufficient points to fit the models or the R^2 between the semi-variogram and the model fit was <0.9 . The large circles are those that passed these tests. The corresponding estimates from Soil Moisture Active Passive sea surface salinity are in cyan (zonal) and pink (meridional) circles. The corresponding estimates from Integrated Multi-satellitE Retrievals for GPM rain rate are in dark blue (zonal) and dark red (meridional).

The SMAP temporal resolution (8-day running mean centered on each day) appears to be too coarse to resolve prominent high-frequency temporal variations of SSS during the rainy season, but SMAP is consistent with in situ estimates in its estimation of integral time scale during the dry season alone (Figure 7). For example, in the rainy season, even the 10th percentile value of the SMAP integral time scale (2–2.5 days) is still larger than the values computed from the in situ moorings (1–2 days). The overestimation of SSS integral time scale by SMAP in the rainy season is expected due to the relative coarseness of the SMAP product, which misses sub-footprint and sub-time step variability. However, during the dry season, the near-surface salinity integral time scale at the central mooring location from both the closest SMAP grid box (solid gray line) and observations (red line with circles) show similar high amplitude swings and similar mean values, between 1 and 5 days, with an average value of about 3 days. The 10th and 90th percentile (gray shading) and mean (black line with circles) of SMAP SSS integral time scale averaged across the SPURS-2 central area and the SMAP value at the central mooring location (solid gray line) stay roughly consistent throughout the year. This indicates that SMAP SSS does not capture the short integral time scale during the rainy season nor its transitions between dry and rainy seasons.

4.3. Length Scales of Variability: Rain and Near-Surface Salinity

The meridional integral length scales from in situ near-surface salinity are about 20 km during the rainy seasons (Figure 8). In the dry season they are more varied and usually longer, ranging from 20 to 100 km. That is, the in situ near-surface salinity distribution is more uniform during the dry season or the variability is on a larger scale. Consistent with this is the fact that the integral time scales increase by at least a factor of 2 during the dry season (Figure 7). The increase represents a shift in spatial patterns and scales of in situ salinity variability from the atmospheric mesoscale during the rainy season to the ocean mesoscale in the dry season.

The zonal integral length scales from in situ near-surface salinity are largely below significance level (Figure 8), except during the rainy seasons at the beginning and end of the experiment. At that time, the scales are about 50 km, much longer than the meridional integral length scales. This is consistent with the ITCZ rainfall being zonally elongated and meridionally constrained, and made up of zonally propagating atmospheric disturbances such as easterly waves (Figure 4).

Figure 7. (a) Integral time scales of near surface salinity and (b) rainfall at the three SPURS-2 moorings—central, North, and South moorings, as well as the mean (black line with circles), 10th and 90th percentiles (blue and gray shaded area) of the integral length scales of satellite rainfall (Integrated Multi-satellitE Retrievals for GPM) and salinity (Soil Moisture Active Passive sea surface salinity) over the SPURS-2 central area (8° – 12° N, 120° – 130° W). The integral time scale is computed each day from a rolling 30-day window centered on the day. Different records are color-coded according to the legend at the top. (c–h) Histograms of the corresponding integral time scales in panels (a, b) except excluding the near surface salinity at North and South moorings.

Note that the availability of data to estimate in situ near-surface salinity integral length scales in Figure 8 depended on the distribution of SPURS-2 salinity platforms in the 30-day moving window (Figure 2). For the in situ near-surface salinity integral length scale estimation in the dry season, the data for computing the meridional semi-variograms were sparse and mostly provided by data from Wave Gliders. For example, a single rainy week in early March decreased the 30-day sliding window estimates of integral length scales for February–March. The mean zonal semi-variograms are more reliable around the time period of the two SPURS-2 cruises in fall 2016 and fall 2017, when dozens of measuring platforms were released in the vicinity of the mooring arrays, that is,—when most Lagrangian platforms had not been carried too far east or west by strong currents (Figures 2 and 8).

SMAP SSS does not capture integral length scales <70 km present in the in situ data at any time, nor the observed contrasts between in situ zonal and meridional spatial decorrelation scales. Because of the intrinsic limitations of estimating salinity from space, the SMAP integral length scale is about 75 km in all seasons and directions (Figure 8), which can be as much as twice the scales estimated from in situ measurements during the rainy season. Oddly though, during the dry season, the meridional integral length scale of SMAP SSS sometimes remains smaller than that of in situ near-surface salinity.

The integral length scale of IMERG rain in both directions and all seasons is about 50 km, which is five times its grid resolution, equal to the in situ salinity zonal integral length scale in the rainy season, and double the meridional in situ salinity scale in the same season. The integral length scales of rain are not computed from in situ data for reasons described in Section 3.2. If the in situ rain data were more numerous and spatially distributed, we suspect that the in situ integral length scales of rainfall would be on the order of the atmospheric mesoscale (O 10–100 km) and perhaps smaller than suggested by IMERG in the dry season. While the IMERG grid resolution is only 10 km, inspection of individual IMERG time step rain maps during SPURS-2 suggest that it does not include or capture features smaller in total size than about 30 km. This 30-km effective spatial resolution of IMERG is consistent with it being based or trained on PMW data that is 15–30 km scale (Chiu et al., 1993; Kummerow, 1998; Wilheit et al., 1991). These scales of input data to IMERG are relatively coarse compared to the 1–10 km diameter of the majority of tropical oceanic rain cells, which are prevalent in all seasons but more dominant in the dry trade wind time period (Cifelli et al., 2007; Schumacher & Houze, 2003; Thompson, Moum, et al., 2019; Trivej & Stevens, 2010). Similar to SMAP, IMERG also noticeably lacks distinction between the meridional versus zonal integral length scales. Even monthly average IMERG precipitation maps in Figure 4 show zonal elongation of rain compared to the meridional direction, which is consistent with ITCZ climatology (e.g., Houze et al., 2015). In summary, the IMERG integral length scale estimates in Figure 8 are not consistent with our in situ salinity integral length scale estimates, visual inspection of the IMERG data, or climatology (e.g., Houze et al., 2015). We do not have an explanation for why IMERG meridional integral length scales are not shorter than zonal scales. The IMERG integral length scale estimates might be more trustworthy in the zonal direction during the rainy season because they are longer than the effective IMERG product resolution (about 30 km).

5. Summary and Conclusions

Understanding and monitoring the spatial and temporal patterns of the hydrologic cycle are key goals of the operational earth observing and prediction systems (Durack, 2015). The NASA SPURS-2 field campaign in situ data are used to better understand the relationship between integral time and length scales of rain and near-surface salinity in the East Pacific Fresh Pool (EPFP), and to comprehensively test satellite data for their ability to accurately determine these integral scales and their seasonal variations. Toward this goal, this work analyzed the NASA SPURS-2 2016–2017 field campaign near-surface salinity together with all available long time series rain rate data in the region. While both rain and SSS can be tracked over tropical oceans with satellite products, few in situ measurements of either quantity exist over the oceans for extended periods of time and at high resolution in a limited region, particularly throughout an entire annual cycle of ocean dynamics and surface freshwater forcing. The SPURS-2 data sets offer a unique opportunity to use in situ observations to quantify and better understand the temporal and spatial scales of variability in rain forcing and near-surface salinity response in the EPFP, and to use these to validate satellite estimates of these metrics.

To quantify and understand the relationships between spatiotemporal variability of rain and near-surface salinity, we compute autocorrelation to obtain integral time scales and semi-variograms for integral length scales. We do this using in situ measurements from the SPURS-2 field campaign (except for integral length scale of rain) as well as the finest-scale global continuous satellite-based products available: 25 km (regridded from 70-km), daily

8-day running mean SMAP SSS, and 10 km, 30-min IMERG rain. In situ results are focused on the south, central, and north mooring locations at 9°, 10°, 11°N along 125°W, while satellite results cover a similar but slightly wider SPURS-2 central area (8°–12°N, 120°–130°W). The integral time and length scales are the decorrelation time and space scales for measured quantities in the flow, that is, how far in time or space that nearby points are still significantly alike.

The integral length and time scales of rain and near-surface salinity vary seasonally. In the rainy low-wind ITCZ season, rain events are frequent, intense, result in significant accumulation, and can occur over wide areas. Wind speed is usually low, 0–8 m/s, whether rain is present or not. Rain is likely to stabilize the upper few meters of the ocean during this time in the form of fresh layers or lenses (Drushka et al., 2019; Reverdin et al., 2020). These stable fresh lenses can outlast their parent rain events if the wind speed is low enough (Thompson, Moun, et al., 2019) or if preexisting stratification below the fresh layer contributes to the stability of the surface layer (Iyer & Drushka, 2021a). Due to this and other ocean processes that redistribute freshwater in the ocean after rainfall, the integral time scale of near-surface salinity is longer than that of rain when the ITCZ is present. The integral time scales of near-surface salinity (1–2 days, ocean submesoscale, low end ocean mesoscale) decrease and approach that of rain during this season, but are still longer than that of rain (30–60 min, atmospheric mesoscale).

Since rain is more organized and long-lived in the ITCZ season, the rain integral time scales are largest at this time of year. Because of the limitations in the spatial distribution of the SPURS-2 in-situ rain data, it was not possible to compute in situ integral length scales of rain, but they are likely larger in the ITCZ time period too. Zonally propagating and -organized rain features in the ITCZ lead to larger in situ zonal integral length scales of near-surface salinity in this time period (50 km) than in the meridional direction (20 km). Both of these near-surface salinity integral length scales are on the low end of the ocean mesoscale (Delcroix et al., 2019). In the dry season, rain events shrink in size, frequency, and accumulation, while persistent northeasterly winds increase to ~8 m/s. Near-surface salinity stratification by rain is less likely in this time period. The integral time scale of rain shrinks to under 30 min (low end of the atmospheric mesoscale) but the near-surface salinity integral time scale grows to 1–5 days (ocean mesoscale). This is due to the larger influence of ocean mesoscale eddies and currents (NEC) in controlling near-surface salinity features and their variability in the dry season at this location (Farrar & Weller, 2006; A. Hasson et al., 2019). There is some indication from in situ near-surface salinity data that its integral length scale increases to over 100 km in the meridional direction at certain times before and after the rainy seasons. Near-surface salinity in situ data coverage was not sufficient to fully describe the entire dry-to-rainy or rainy-to-dry season transitions in terms of integral length scales.

Our ability to describe the in situ scales of spatiotemporal variability using satellite IMERG rain and SMAP SSS products also varies with season since the observed in situ integral length and time scales can dip below the resolution of each satellite product. Ocean sub-mesoscale to low end mesoscale variability of SSS in the rainy season is not well-captured by SMAP, which shows mean and even 10th percentile SSS integral time scales larger than the observed in situ scales of 1–2 days. SMAP also cannot detect the observed low-end ocean mesoscale integral length scales of SSS in either meridional or zonal direction, nor the fact that the zonal scale is twice as large as the meridional, in the rainy season. Instead, SMAP integral length scales are ~75 km in the rainy season, matching the product's intrinsic resolution. The SMAP SSS estimates of integral time and length scales are consistent with those from in situ observations in the dry trade wind time period when SSS is dominated by ocean mesoscale processes which are larger than the resolution of the SMAP product. The rain integral time scale, which is on the atmospheric mesoscale in both seasons according to in situ data, is overestimated by a factor of two to ten by IMERG in both seasons. However, the IMERG rain integral time scale does correctly capture the observed trend of decreasing rain time scale in the dry season. The IMERG rain integral length scale was estimated to be ~50 km in both zonal and meridional directions throughout the year. Since this value is equal to the integral length scale of in situ near-surface salinity in the zonal direction in the rainy season, and the integral time scales of rain and SSS also converge at that time, IMERG may be suitable for estimating *zonal* integral length scale in the ITCZ season. However, based on IMERG's inability to capture features <30 km total dimension and the results of integral time scale analysis, we expect IMERG might be too coarse to resolve shorter integral length scales in the dry season or in the rainy season for the meridional direction. These results guide interpretation on the extent to which satellite observations of rain and SSS can be used to deduce spatial and temporal patterns of the hydrologic cycle in the EPPF and potentially also other ITCZ regions.

Data Availability Statement

The complete SPURS-2 salinity and meteorological data set stated in Table 1 are from <https://podaac.jpl.nasa.gov/cloud-datasets?search=spurs2>. Central (WHOI) mooring CTD and meteorological data: Farrar, J.T. SPURS Field Campaign SPURS Central Mooring Products. Ver. 1.0. PO.DAAC, CA, USA. accessed [2021-01-26] at <https://doi.org/10.5067/SPUR2-MOOR1>. PMEL profiling CTD (PICO) mooring data: Zhang, D, Kessler, W.S. SPURS Field Campaign Pico Mooring Data Products. Ver. 1.0. PO.DAAC, CA, USA. accessed [2019-11-14] at <https://doi.org/10.5067/SPUR2-MOOR2>. Mixed Layer Lagrangian float data: Andrey Shcherbina. SPURS-2 Field Campaign Neutrally Buoyant Float Data Products. Ver. 1.0. PO.DAAC, CA, USA. accessed [2019-09-18] at <https://doi.org/10.5067/SPUR2-NBFLT>. Surface drifter data: L. Centurioni, V. Hormann, G. Reverdin, A. Hasson, A. Supply, D. Volkov. SPURS Field Campaign Drifter Data Products. Ver. 1.0. PO.DAAC, CA, USA. accessed [2019-10-08] at <https://doi.org/10.5067/SPUR2-DRIFT>. Seaglider data: Luc Rainville. SPURS-2 Field Campaign Waveglider Data Products. Ver. 1.0. PO.DAAC, CA, USA. accessed [2019-10-17] at <https://doi.org/10.5067/SPUR2-GLID1>. Waveglider data: Ben Hodges. SPURS-2 Field Campaign Waveglider Data Products. Ver. 1.0. PO.DAAC, CA, USA. accessed [2019-07-25] at <https://doi.org/10.5067/SPUR2-GLID3>. Saildrone data: D. Zhang, and M.F. Cronin. SPURS Field Campaign ARGO float Products. Ver. 1.0. PO.DAAC, CA, USA. accessed [2019-03-29] at <https://doi.org/10.5067/SPUR2-SDRON>. Surface salinity snake data: Julian Schanze. SPURS Field Campaign Salinity Snake Products. Ver. 1.0. PO.DAAC, CA, USA. accessed [2019-11-11] at <https://doi.org/10.5067/SPUR2-SNAKE>. Surface salinity profiler (SSP) data: Drushka, K., E. Thompson and W. Asher. SPURS-2 Field Campaign Surface Salinity Profiler Data Products. Ver. 1.0. PO.DAAC, CA, USA. accessed [2019-10-17] at <https://doi.org/10.5067/SPUR2-SSP00>. Underway salinity profiling system (USPS) data: Asher, W., E. Thompson and K. Drushka. SPURS Field Campaign USPS Products. Ver. 1.0. PO.DAAC, CA, USA. accessed [2019-08-02] at <https://doi.org/10.5067/SPUR2-USPS0>. Lady Amber profiling system (LAPS) data: Drushka, K., W. Asher, J. Schanze and L. Rainville. SPURS Field Campaign PALS Products. Ver. 1.0. PO.DAAC, CA, USA. accessed [2019-09-27] at <https://doi.org/10.5067/SPUR2-LAMBR>. The IMERG data were provided by the NASA/Goddard Space Flight Center's Mesoscale Atmospheric Processes Laboratory and PPS and available at the NASA GES DISC via <https://pmm.nasa.gov/data-access/downloads/gpm>. Remote Sensing Systems (RSS). 2022. SMAP Sea Surface Salinity Products. Ver. 5.0. PO.DAAC, CA, USA. Data set accessed [2022-04-19] at <https://doi.org/10.5067/SMP50-3SPCS> (Meissner et al., 2022).

Acknowledgments

This work was funded by NASA Physical Oceanography under the SPURS-2 Synthesis Grant 80NSSC18K1499 for A. Shcherbina (principal investigator), L. Rainville, E. Thompson, and N. Chi; the NOAA/NASA Interagency Agreement, NASA Ocean Salinity Science Team agreement number 80HQTR20T0046 for H. Chen and E. Thompson (principal investigator); and the NASA SPURS-2 Information System Grant 80NSSC18K0809 for F. Bingham. SPURS-2 research and data collection were made possible by the NASA Ocean Salinity Science Team. We acknowledge the large team of scientists, engineers, technicians, managers, ship crew, and data archivists that were responsible for the SPURS-2 field experiment. We thank the two anonymous reviewers for their valuable comments and suggestions.

References

- Alory, G., Maes, C., Delcroix, T., Reul, N., & Illig, S. (2012). Seasonal dynamics of sea surface salinity off Panama: The far Eastern Pacific Fresh Pool. *Journal of Geophysical Research*, *117*(C4), C04028. <https://doi.org/10.1029/2011JC007802>
- Amador, J. A., Alfaro, E. J., Lizano, O. G., & Magaña, V. O. (2006). Atmospheric forcing of the eastern tropical Pacific: A review. *Progress in Oceanography*, *69*(2–4), 101–142. <https://doi.org/10.1016/j.pocean.2006.03.007>
- Asher, W., Thompson, E., & Drushka, K. (2019). SPURS field campaign USPS products. Ver. 1.0 [Dataset]. PO.DAAC. <https://doi.org/10.5067/SPUR2-USPS0>
- Bao, S., Wang, H., Zhang, R., Yan, H., & Chen, J. (2019). Comparison of satellite-derived sea surface salinity products from SMOS, Aquarius, and SMAP. *Journal of Geophysical Research: Oceans*, *124*(3), 1932–1944. <https://doi.org/10.1029/2019JC014937>
- Baumgartner, A., & Reichel, E. (1975). *World Water Balance: Mean annual global, continental and maritime precipitation, evaporation and run-off*. Elsevier.
- Bingham, F. M. (2019). Subfootprint variability of sea surface salinity observed during the SPURS-1 and SPURS-2 field campaigns. *Remote Sensing*, *11*(22), 2689. <https://doi.org/10.3390/rs11222689>
- Bingham, F. M., & Lee, T. (2017). Space and time scales of sea surface salinity and freshwater forcing variability in the global ocean (60°S–60°N). *Journal of Geophysical Research: Oceans*, *122*(4), 2909–2922. <https://doi.org/10.1002/2016JC012216>
- Bingham, F. M., Tsontos, V., deCharon, A., Lauter, C. J., & Taylor, L. (2019). The SPURS-2 eastern tropical Pacific field campaign data collection. *Oceanography*, *32*(2), 142–149. <https://doi.org/10.5670/oceanog.2019.222>
- Centurioni, L., Hormann, V., Reverdin, G., Hasson, A., Supply, A., & Volkov, D. (2019). SPURS field campaign drifter data products. Ver. 1.0 [Dataset]. PO.DAAC. <https://doi.org/10.5067/SPUR2-DRIFT>
- Chiu, L. S., Chang, A. T. C., & Janowiak, J. (1993). Comparison of monthly rain rates derived from GPI and SSM/I using probability distribution functions. *Journal of Applied Meteorology and Climatology*, *32*(2), 323–334. [https://doi.org/10.1175/1520-0450\(1993\)032<0323:COMRRD>2.0.CO;2](https://doi.org/10.1175/1520-0450(1993)032<0323:COMRRD>2.0.CO;2)
- Cifelli, R., Nesbitt, S. W., Rutledge, S. A., Petersen, W. A., & Yuter, S. (2007). Radar characteristics of precipitation features in the EPIC and TEPPS regions of the east Pacific. *Monthly Weather Review*, *135*(4), 1576–1595. <https://doi.org/10.1175/MWR3340.1>
- Cifelli, R., Nesbitt, S. W., Rutledge, S. A., Petersen, W. A., & Yuter, S. (2008). Diurnal characteristics of precipitation features over the east Pacific: A comparison of the EPIC and TEPPS regions. *Journal of Climate*, *21*(16), 4068–4086. <https://doi.org/10.1175/2007JCLI2020.1>
- Clayton, C. A., Edson, J. B., Paget, A., Graham, R., & Greenwood, B. (2019). Effects of rainfall on the atmosphere and the ocean during SPURS-2. *Oceanography*, *32*(2), 86–97. <https://doi.org/10.5670/oceanog.2019.216>
- Cressie, N., & Hawkins, D. M. (1980). Robust estimation of the variogram. I. *Mathematical Geology*, *12*(2), 115–125. <https://doi.org/10.1007/BF01035243>

- Delcroix, T., Chaigneau, A., Soviadan, D., Boutin, J., & Pegliasco, C. (2019). Eddy-induced salinity changes in the tropical Pacific. *Journal of Geophysical Research: Oceans*, *124*(1), 374–389. <https://doi.org/10.1029/2018JC014394>
- Doney, S. C., Glover, D. M., McCue, S. J., & Fuentes, M. (2003). Mesoscale variability of Sea-viewing Wide Field-of-view Sensor (SeaWiFS) satellite ocean color: Global patterns and spatial scales. *Journal of Geophysical Research*, *108*(C2), 3024. <https://doi.org/10.1029/2001JC000843>
- Drucker, R., & Riser, S. C. (2014). Validation of Aquarius sea surface salinity with Argo: Analysis of error due to depth of measurement and vertical salinity stratification. *Journal of Geophysical Research: Oceans*, *119*(7), 4626–4637. <https://doi.org/10.1002/2014JC010045>
- Drushka, K., Asher, W., Schanze, J., & Rainville, L. (2019). SPURS field campaign PALS products. Ver. 1.0 [Dataset]. PO.DAAC. <https://doi.org/10.5067/SPUR2-LAMBR>
- Drushka, K., Asher, W. E., Jessup, A. T., Thompson, E. J., Iyer, S., & Clark, D. (2019). Capturing fresh layers with the surface salinity profiler. *Oceanography*, *32*(2), 76–85. <https://doi.org/10.5670/oceanog.2019.215>
- Drushka, K., Asher, W. E., Ward, B., & Walesby, K. (2016). Understanding the formation and evolution of rain-formed fresh lenses at the ocean surface. *Journal of Geophysical Research: Oceans*, *121*(4), 2673–2689. <https://doi.org/10.1002/2015JC011527>
- Drushka, K., Thompson, E., & Asher, W. (2019). SPURS-2 field campaign surface salinity profiler data products. Ver. 1.0 [Dataset]. PO.DAAC. <https://doi.org/10.5067/SPUR2-SSP00>
- Durack, P. J. (2015). Ocean salinity and the global water cycle. *Oceanography*, *28*(1), 20–31. <https://doi.org/10.5670/oceanog.2015.03>
- Farrar, J. T. (2020). SPURS field campaign SPURS central mooring products. Ver. 1.0 [Dataset]. PO.DAAC. <https://doi.org/10.5067/SPUR2-MOORI>
- Farrar, J. T., & Plueddemann, A. J. (2019). On the factors driving upper-ocean salinity variability at the western edge of the Eastern Pacific Fresh Pool. *Oceanography*, *32*(2), 30–39. <https://doi.org/10.5670/oceanog.2019.209>
- Farrar, J. T., & Weller, R. A. (2006). Intraseasonal variability near 10°N in the eastern tropical Pacific Ocean. *Journal of Geophysical Research*, *111*(C5), C05015. <https://doi.org/10.1029/2005JC002989>
- Fiedler, P. C., & Talley, L. D. (2006). Hydrography of the eastern tropical Pacific: A review. *Progress in Oceanography*, *69*(2–4), 143–180. <https://doi.org/10.1016/j.pocean.2006.03.008>
- Guimbard, S., Reul, N., Chapron, B., Umbert, M., & Maes, C. (2017). Seasonal and interannual variability of the Eastern Tropical Pacific Fresh Pool. *Journal of Geophysical Research: Oceans*, *122*(3), 1749–1771. <https://doi.org/10.1002/2016JC012130>
- Hasson, A., Farrar, J. T., Boutin, J., Bingham, F., & Lee, T. (2019). Intraseasonal variability of surface salinity in the eastern tropical Pacific associated with mesoscale eddies. *Journal of Geophysical Research: Oceans*, *124*(4), 2861–2875. <https://doi.org/10.1029/2018JC014175>
- Hasson, A. E. A., Delcroix, T., & Dussin, R. (2013). An assessment of the mixed layer salinity budget in the tropical Pacific Ocean. Observations and modelling (1990–2009). *Ocean Dynamics*, *63*(2–3), 179–194. <https://doi.org/10.1007/s10236-013-0596-2>
- Hodges, B. (2019). SPURS-2 field campaign waveglider data products. Ver. 1.0 [Dataset]. PO.DAAC. <https://doi.org/10.5067/SPUR2-GLID3>
- Houze, R. A., Rasmussen, K. L., Zuluaga, M. D., & Brodzik, S. R. (2015). The variable nature of convection in the tropics and subtropics: A legacy of 16 years of the tropical rainfall measuring mission satellite. *Reviews of Geophysics*, *53*(3), 994–1021. <https://doi.org/10.1002/2015RG000488>
- Huffman, G. J., Bolvin, D. T., Braithwaite, D., Hsu, K., Joyce, R., Kidd, C., et al. (2019). NASA global precipitation measurement (GPM) integrated multi-satellite retrievals for GPM (IMERG) [Dataset]. Algorithm Theoretical Basis Document (ATBD) Version 06, 38. Retrieved from https://gpm.nasa.gov/sites/default/files/document_files/IMERG_ATBD_V06.pdf
- Huffman, G. J., Bolvin, D. T., Braithwaite, D., Hsu, K., Joyce, R., Kidd, C., et al. (2020). Integrated multi-satellite retrievals for the global precipitation measurement (GPM) mission (IMERG). In V. Levizzani, C. Kidd, D. Kirschbaum, C. Kummerow, K. Nakamura, & F. J. Turk (Eds.), *Chapter 19 in adv. Global change res., vol. 67, satellite precipitation measurement* (pp. 343–353). Springer Nature.
- Iyer, S., & Drushka, K. (2021a). The influence of preexisting stratification and tropical rain modes on the mixed layer salinity response to rainfall. *Journal of Geophysical Research: Oceans*, *126*(10), e2021JC017574. <https://doi.org/10.1029/2021JC017574>
- Iyer, S., & Drushka, K. (2021b). Turbulence within rain-formed fresh lenses during the SPURS-2 experiment. *Journal of Physical Oceanography*, *51*(5), 1705–1721. <https://doi.org/10.1175/JPO-D-20-0303.1>
- Journel, A. G., & Huijbregts, C. J. (1978). *Mining geostatistics* (p. 600). Academic Press.
- Kao, H.-Y., Lagerloef, G. S. E., Lee, T., Melnichenko, O., Meissner, T., & Hacker, P. (2018). Assessment of Aquarius sea surface salinity. *Remote Sensing*, *10*(9), 1341. <https://doi.org/10.3390/rs10091341>
- Kitanidis, P. K. (1997). *Introduction to geostatistics: Applications in hydrogeology* (p. 249). Cambridge University Press.
- Kummerow, C. (1998). Beamfilling errors in passive microwave rainfall retrievals. *Journal of Applied Meteorology*, *37*(4), 356–370. [https://doi.org/10.1175/1520-0450\(1998\)037<0356:BEIPMR>2.0.CO;2](https://doi.org/10.1175/1520-0450(1998)037<0356:BEIPMR>2.0.CO;2)
- Lindstrom, E. J., Edson, J. B., Schanze, J. J., & Shcherbina, A. Y. (2019). SPURS-2: Salinity processes in the upper-ocean regional study 2 – The eastern equatorial Pacific experiment. *Oceanography*, *32*(2), 15–19. <https://doi.org/10.5670/oceanog.2019.207>
- Meissner, T., Wentz, F. J., & Le Vine, D. M. (2018). The salinity retrieval algorithms for the NASA Aquarius version 5 and SMAP version 3 releases. *Remote Sensing*, *10*(7), 1121. <https://doi.org/10.3390/rs10071121>
- Meissner, T., Wentz, F. J., Manaster, A., Lindsley, R., Brewer, M., & Densberger, M. (2022). Remote sensing systems SMAP ocean surface salinities [level 3 running 8-day], version 5.0 validated release [Dataset]. Remote Sensing Systems. <https://doi.org/10.5067/SMP50-3SPCS>
- Melnichenko, O., Hacker, P., Bingham, F. M., & Lee, T. (2019). Patterns of SSS variability in the eastern tropical Pacific: Intraseasonal to inter-annual timescales from seven years of NASA satellite data. *Oceanography*, *32*(2), 20–29. <https://doi.org/10.5670/oceanog.2019.208>
- O, S., Foelsche, U., Kirchengast, G., Fuchsberger, J., Tan, J., & Petersen, W. A. (2017). Evaluation of GPM IMERG Early, Late, and Final rainfall estimates using WegenerNet gauge data in southeastern Austria. *Hydrology and Earth System Sciences*, *21*(12), 6559–6572. <https://doi.org/10.5194/hess-21-6559-2017>
- Olmedo, E., González-Haro, C., Hoareau, N., Umbert, M., González-Gambau, V., Martínez, J., et al. (2021). Nine years of SMOS sea surface salinity global maps at the Barcelona Expert Center. *Earth System Science Data*, *13*(2), 857–888. <https://doi.org/10.5194/essd-13-857-2021>
- Petersen, W. A., Cifelli, R., Boccippio, D. J., Rutledge, S. A., & Fairall, C. (2003). Convection and easterly wave structure observed in the eastern Pacific warm-pool during EPIC-2001. *Journal of the Atmospheric Sciences*, *60*(15), 1754–1773. [https://doi.org/10.1175/1520-0469\(2003\)060<1754:CAEWSO>2.0.CO;2](https://doi.org/10.1175/1520-0469(2003)060<1754:CAEWSO>2.0.CO;2)
- Qin, S., Wang, H., Zhu, J., Wang, H., & Zhang, Y. (2020). Validation and correction of sea surface salinity retrieval from SMAP. *Acta Oceanologica Sinica*, *39*(3), 148–158. <https://doi.org/10.1007/s13131-020-1533-0>
- Rainville, L. (2019). SPURS-2 field campaign waveglider data products. Ver. 1.0 [Dataset]. PO.DAAC. <https://doi.org/10.5067/SPUR2-GLID1>
- Rainville, L., Centurioni, L. R., Asher, W. E., Clayson, C. A., Drushka, K., Edson, J. B., et al. (2019). Novel and flexible approach to access the open ocean: Uses of sailing research vessel Lady Amber during SPURS-2. *Oceanography*, *32*(2), 116–121. <https://doi.org/10.5670/oceanog.2019.219>
- Reverdin, G., Morisset, S., Boutin, J., & Martin, N. (2012). Rain-induced variability of near sea-surface T and S from drifter data. *Journal of Geophysical Research*, *117*(C2), C02032. <https://doi.org/10.1029/2011JC007549>

- Reverdin, G., Supply, A., Drushka, K., Thompson, E. J., Asher, W. E., & Lourenço, A. (2020). Intense and small freshwater pools from rain-fall investigated during SPURS-2 on 9 November 2017 in the eastern tropical Pacific. *Journal of Geophysical Research: Oceans*, 125(2), e2019JC015558. <https://doi.org/10.1029/2019JC015558>
- Riser, S. C., Yang, J., & Drucker, R. (2019). Observations of large-scale rainfall, wind, and sea surface salinity variability in the eastern tropical Pacific. *Oceanography*, 32(2), 42–49. <https://doi.org/10.5670/oceanog.2019.211>
- Rutledge, S. A., Chandrasekar, V., Fuchs, B., George, J., Junyent, F., Kennedy, P., & Dolan, B. (2019). Deployment of the SEA-POL C-band polarimetric radar to SPURS-2. *Oceanography*, 32(2), 50–57. <https://doi.org/10.5670/oceanog.2019.212>
- Schanze, J. (2019). SPURS field campaign salinity snake products. Ver. 1.0 [Dataset]. PO.DAAC. <https://doi.org/10.5067/SPUR2-SNAKE>
- Schanze, J. J., Schmitt, R. W., & Yu, L. L. (2010). The global oceanic freshwater cycle: A state-of-the-art quantification. *Journal of Marine Research*, 68(3), 569–595. <https://doi.org/10.1357/002224010794657164>
- Schumacher, C., & Houze, R. A., Jr. (2003). The TRMM precipitation radar's view of shallow, isolated rain. *Journal of Applied Meteorology*, 42(10), 1519–1524. [https://doi.org/10.1175/1520-0450\(2003\)042<1519:TTPRVO>2.0.CO;2](https://doi.org/10.1175/1520-0450(2003)042<1519:TTPRVO>2.0.CO;2)
- Schwanghar, W. (2020). variogramfit. [Software]. MATLAB Central File Exchange. Retrieved from <https://www.mathworks.com/matlabcentral/fileexchange/25948-variogramfit>
- Shcherbina, A. (2019). SPURS-2 field campaign neutrally buoyant float data products. Ver. 1.0 [Dataset]. PO.DAAC. <https://doi.org/10.5067/SPUR2-NBFLT>
- Shcherbina, A. Y., D'Asaro, E. A., & Harcourt, R. R. (2019). Rain and sun create slippery layers in the Eastern Pacific Fresh Pool. *Oceanography*, 32(2), 98–107. <https://doi.org/10.5670/oceanog.2019.217>
- Skofronick-Jackson, G., Petersen, W. A., Berg, W., Kidd, C., Stocker, E. F., Kirschbaum, D. B., et al. (2017). The global precipitation measurement (GPM) mission for science and society. *Bulletin of the American Meteorological Society*, 98(8), 1679–1695. <https://doi.org/10.1175/BAMS-D-15-00306.1>
- Sprintall, J. (2019). Upper ocean salinity stratification during SPURS-2. *Oceanography*, 32(2), 40–41. <https://doi.org/10.5670/oceanog.2019.210>
- Supply, A., Boutin, J., Reverdin, G., Vergely, J.-L., & Bellenger, H. (2020). Variability of satellite sea surface salinity under rainfall. In V. Levizzani, C. Kidd, D. Kirschbaum, C. Kummerow, K. Nakamura, & F. Turk (Eds.), *Satellite precipitation measurement, advances in global change research* (Vol. 69, pp. 1155–1176). Springer Nature. (Chapter 58). https://doi.org/10.1007/978-3-030-35798-6_34
- Supply, A., Boutin, J., Vergely, J.-L., Martin, N., Hasson, A., Reverdin, G., et al. (2017). Precipitation estimates and L-band sea surface salinity (PEALS). *Quarterly Journal of the Royal Meteorological Society*, 144(S1), 103–119. <https://doi.org/10.1002/qj.3110>
- Tang, W., Fore, A., Yueh, S., Lee, T., Hayashi, A., Sanchez-Franks, A., et al. (2017). Validating SMAP SSS with in-situ measurements. *Remote Sensing of Environment*, 200, 326–340. <https://doi.org/10.1016/j.rse.2017.08.021>
- Thompson, E. J., Asher, W. E., Jessup, A. T., & Drushka, K. (2019). High-resolution rain maps from an X-band marine radar and their use in understanding ocean freshening. *Oceanography*, 32(2), 58–65. <https://doi.org/10.5670/oceanog.2019.213>
- Thompson, E. J., Moum, J. N., Fairall, C. W., & Rutledge, S. A. (2019). Wind limits on rain layers and diurnal warm layers. *Journal of Geophysical Research: Oceans*, 124(2), 897–924. <https://doi.org/10.1029/2018JC014130>
- Trenberth, K. E., Smith, L., Qian, T., Dai, A., & Fasullo, J. (2007). Estimates of the global water budget and its annual cycle using observational and model data. *Journal of Hydrometeorology*, 8(4), 758–769. <https://doi.org/10.1175/JHM600.1>
- Trivej, P., & Stevens, B. (2010). The echo size distribution of precipitating shallow Cumuli. *Journal of the Atmospheric Sciences*, 67(3), 788–804. <https://doi.org/10.1175/2009JAS3178.1>
- Tzortzi, E., Srokosz, M., Gommenginger, C., & Josey, S. A. (2016). Spatial and temporal scales of variability in Tropical Atlantic sea surface salinity from the SMOS and Aquarius satellite missions. *Remote Sensing of Environment*, 180, 418–430. <https://doi.org/10.1016/j.rse.2016.02.008>
- Villarini, G., & Krajewski, W. F. (2007). Evaluation of the research-version TMPA three-hourly 0.25°x0.25° rainfall estimates over Oklahoma. *Geophysical Research Letters*, 34(5), L05402. <https://doi.org/10.1029/2006GL029147>
- Vinogradova, N., Lee, T., Boutin, J., Drushka, K., Fournier, S., Sabia, R., et al. (2019). Satellite salinity observing system: Recent discoveries and the way forward. *Frontiers in Marine Science*, 6, 243. <https://doi.org/10.3389/fmars.2019.00243>
- Vinogradova, N. T., & Ponte, R. M. (2017). In search of fingerprints of the recent intensification of the ocean water cycle. *Journal of Climate*, 30(14), 5513–5528. <https://doi.org/10.1175/JCLI-D-16-0626.1>
- Volkov, D. L., Dong, S., Foltz, G. R., Goni, G., & Lumpkin, R. (2019). Observations of near-surface salinity and temperature structure with dual-sensor Lagrangian drifters during SPURS-2. *Oceanography*, 32(2), 66–75. <https://doi.org/10.5670/oceanog.2019.214>
- Wilheit, T. T., Chang, A. T., & Chiu, L. S. (1991). Retrieval of monthly rainfall indices from microwave radiometric measurements using probability distribution functions. *Journal of Atmospheric and Oceanic Technology*, 8(1), 118–136. [https://doi.org/10.1175/1520-0426\(1991\)008<0118:ROMRIF>2.0.CO;2](https://doi.org/10.1175/1520-0426(1991)008<0118:ROMRIF>2.0.CO;2)
- Yu, L. (2015). Sea-surface salinity fronts and associated salinity-minimum zones in the tropical ocean. *Journal of Geophysical Research: Oceans*, 120(6), 4205–4225. <https://doi.org/10.1002/2015JC010790>
- Zhang, D., & Cronin, M. F. (2019). SPURS field campaign ARGO float products. Ver. 1.0 [Dataset]. PO.DAAC. <https://doi.org/10.5067/SPUR2-SDRON>
- Zhang, D., Cronin, M. F., Meinig, C., Farrar, J. T., Jenkins, R., Peacock, D., et al. (2019). Comparing air-sea flux measurements from a new unmanned surface vehicle and proven platforms during the SPURS-2 field campaign. *Oceanography*, 32(2), 122–133. <https://doi.org/10.5670/oceanog.2019.220>
- Zhang, D., & Kessler, W. S. (2019). SPURS field campaign Pico mooring data products. Ver. 1.0 [Dataset]. PO.DAAC. <https://doi.org/10.5067/SPUR2-MOOR2>